Micro- and Nanopillar Chips for Continuous Separation of Extracellular Vesicles

Hattori, Yuya
Department of Biomolecular Engineering, Graduate School of Engineering, Nagoya University

嶋田, 泰祐
Department of Biomolecular Engineering, Graduate School of Engineering, Nagoya University

安井, 隆雄
Department of Biomolecular Engineering, Graduate School of Engineering, Nagoya University

Kaji, Noritada
JST, PRESTO

他

出版情報：Analytical Chemistry. 91 (10), pp.6514-6521, 2019-04-29. American Chemical Society
バージョン：
権利関係：

Micro- and Nanopillar Chips for Continuous Separation of Extracellular Vesicles

Yuya Hattori[†‡], Taisuke Shimada[†‡], Takao Yasui[†‡§], Noritada Kaji[*§∥] and Yoshinobu Baba[†‡⊥#]

[†]Department of Biomolecular Engineering, Graduate School of Engineering, Nagoya University, Furo-cho, Chikusa-ku, Nagoya 464-8603, Japan

[‡]ImPACT Research Center for Advanced Nanobiodevices, Nagoya University, Furo-cho, Chikusa-ku, Nagoya 464-8603, Japan

[§]JST, PRESTO, 4-1-8 Honcho, Kawaguchi, Saitama, 332-0012, Japan

[∥]Department of Applied Chemistry, Graduate School of Engineering, Kyushu University, 744 Motooka, Nishi-ku, Fukuoka 819-0395, Japan

[⊥]Health Research Institute, National Institute of Advanced Industrial Science and Technology (AIST), Hayashi-cho 2217-14, Takamatsu 761-0395, Japan

[#]School of Pharmacy, College of Pharmacy, Kaohsiung Medical University, 100, Shih-Chuan 1st Rd., Kaohsiung, 807, Taiwan, R.O.C.

ABSTRACT: Micro- and nanopillar chips are widely used to separate and enrich biomolecules, such as DNA, RNA, protein, and cells, as an analytical technique and to provide a confined nanospace for polymer science analyses. Herein, we demonstrated a continuous accurate and precise separation technique for extracellular vesicles (EVs)—nanometer-sized vesicles (typically 50–200 nm) currently recognized as novel biomarkers present in biofluids—based on the principle of electroosmotic flow-driven deterministic lateral displacement in micro- and nanopillar array chips. Notably, the easy-to-operate flow control afforded by electroosmotic flow allowed nanoparticles 50–500 nm in size, including EVs, to be precisely separated and enriched in a continuous manner. By observation of the flow behavior of nanoparticles, we found that electroosmotic flow velocity in the nanopillar arrays did not solely depend on counterion mobility on the surface of nanopillar chips but rather showed a parabolic flow profile. This hydrodynamic pressure-free and easy-to-use separation and enrichment technique, which requires only electrode insertion into the reservoirs and electric field application, may thus serve as a promising technique for future precise and accurate EV analysis reflecting both size and composition for research and potential clinical diagnostic applications.

Extracellular vesicles (EVs), which were initially thought to be cellular debris, are now increasingly recognized as promising biomarkers of various diseases as these small vesicles (typically 50–200 nm in diameter for exosomes) contain intracellular information in the form of proteins[1-3], mRNA/miRNA[4-6], and DNA[7, 8]. A significant advantage of EVs as biomarkers of disease is their abundance and stability in any type of biofluid, such as blood, urine, saliva, and breast milk. Moreover, these phospholipid-surrounded vesicles that are secreted by a variety of mammalian cells, circulate throughout the whole body to serve as long-range intercellular communication tools. EVs in non-invasive biofluid samples such as urine are expected to be especially valuable as biomarkers for longitudinal cancer monitoring as both tumor cells and their surrounding cells secrete EVs. Thus, EV analysis may help diagnose tumor type and stage along with response to medicinal treatment[9]. However, the lack of precise preparation and analytical technologies has forestalled the clinical translation of EV assessment.

EVs essentially comprise diverse and heterogeneous nanoparticles released from cells. Owing to the lack of precise separation and measurement techniques, assignment of EV types based on their morphologies is almost impossible and further biochemical assays using antibodies or polymerase chain reaction (PCR) are required, which constitute destructive or modifying analyses. Therefore, there is a need to develop accurate and precise separation, enrichment, and recovery techniques of EVs from biofluids to facilitate their clinical application. Ultracentrifugation and gradient ultracentrifugation methods, considered to be the current gold standard, deliver EVs with a relatively high purity but require lengthy procedures of over 4 h, large sample volumes, and further purification in some cases because of contamination issues, such as with chylomicrons and chemokines[10]. Co-precipitation methods that rely on polymer co-precipitation strategies have also been developed for EV enrichment and several kits (e.g., ExoQuick and Exo-Spin) are already commercially available. Although the kits are easy to use, they are too expensive for large-scale use and their specificity for EVs is not satisfactory. As an alternative, size-exclusion chromatography using commercial columns is being developed but requires process optimization to improve efficiency and resolution of the separation depending on the research demands[11]. More recently, microfluidic filtering techniques have been developed to improve isolation efficiency and specificity. Although the throughput of most of these new methods is too low to support practical use, they indicate the potential of such analytical platforms in providing single-particle EV analysis, e.g., in combination with nanopore sensors. Moreover, most existing technologies face serious challenges especially with regards to exosome extraction, as contamination issues and loss of important size information occurs[12, 13].

EVs are generated through several routes, although the exact mechanisms are still largely unknown. Generally, exosomes are produced through the inward invagination of endosomal membranes, during which various cellular components, such as cytosolic contents, transmembrane and peripheral proteins, and miRNAs, are incorporated. The released vesicles exhibit diameters of 40–200 nm. Other types of EVs, such as microvesicles, are derived from outward budding of the plasma membrane, yielding sizes ranging from 200 to 2,000 nm—albeit with a similar density as exosomes of 1.16–1.19 g/mL. Therefore, separation techniques for EVs smaller or larger than 200 nm in diameter are urgently in demand for the field of EV research.

Deterministic lateral displacement (DLD) pillar arrays are strong candidates for the separation and enrichment of exosomes from EVs depending on size. Huang et al.[14] originally proposed the principle and demonstrated μm-scale particle separation of parasites[15], bacteria[16], blood cells[17], and circulating tumor cells in blood[18]. More recently, separation of EVs as nm-scale particles was first demonstrated by Wunsch et al.[19] using nm-scale lateral displacement (nano-DLD). This method, which utilizes pillar gap sizes ranging from 25 to 235 nm, achieved the separation of a mixture of 50 and 110 nm polystyrene beads and EVs < 100 nm in diameter. However, more than 200 kPa of input pressure was required to transport the beads or EVs through the nanopillar array. Such a high-pressure range in excess of several hundred kPa limits the application potential of this method as a practical tool for EV separation and quantification. Therefore, in the present study, we applied electroosmotic flow (EOF) to drive micro- and nanofluids in micro- and nanopillar chips to facilitate future practical applications as shown in Figure 1.

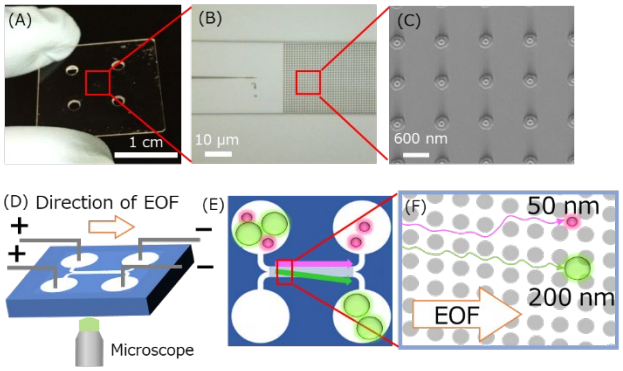

Figure. 1. Micro- and nanopillar chip for EOF-driven DLD. (A) Photo of the nanopillar chip. (B) Magnified optical microscopy image and (C) scanning electron microscopy image. (D–F) Working principle of the nanopillar chip. EOF transports nm-scale objects in a bumping mode (200-nm green beads) or a zigzag mode (50-nm red beads) based on the angle of the nanopillar array.

Based on the DLD principle, we designed micropillar (2.6 μm pillar gap, 2.4 μm pillar diameter, and 1.0 μm pillar height; Supplemental Figure S1) and nanopillar (830 nm pillar gap, 470 nm pillar diameter, and 1.0 μm pillar height; Supplemental Figure S2) chips driven by EOF for the separation of nm-scale objects including EVs by simply applying an electric field through the reservoirs. The EOF profile in the chip was observed and carefully tuned to establish a sheath flow for sample injection. Based on the results, separation conditions were optimized and separation of polystyrene beads was performed. A mixture of 200 and 500-nm beads was separated by the micropillar chip and samples collected at the outlets were confirmed by fluorescence observation, micropore-based particle counter (qNano®) assessment, and scanning electron microscopy (SEM). The nanopillar chip was then applied for separation of a mixture of 50 and 200-nm beads as well as exosomes. Successful separations were achieved even under relatively mild conditions of approximately 100 V/cm with a straightforward procedure.

EXPERIMENTAL SECTION

Device fabrication. Prior to the fabrication of micro- and nanopillar chips, double side polished quartz substrates (20 × 20 × 0.5 mm; Crystal Base Co., Ltd., Osaka, Japan) were washed in piranha solution consisting of a 4:1 mixture of concentrated sulfuric acid (H_2SO_4) with hydrogen peroxide (H_2O_2), at 180 °C for 2 h. **Caution**: *Piranha solution reacts violently with most organic materials and must be handled with extreme care.* For fabrication of the micropillar chips, a chromium layer of approximately 100 nm was deposited on the washed quartz substrate using a quick coater (Mini Quick Coater SC-701 Mk II, Sanyu Electron Co., Ltd., Tokyo, Japan). Then, a positive type photoresist, OFPR-8600LB (Tokyo Ohka Kogyo Co., Ltd., Kawasaki, Japan), was spin coated at 500 rpm for 10 s followed by 1500 rpm for 120 s. After heating the substrate at 95 °C for 5 min on a hot plate to completely evaporate solvents in the photoresist and stabilizer, the photoresist was exposed to the g-line of a mercury lamp through a designed chromium photomask. The exposed microchannel pattern was developed in NMD-3 (Tokyo Ohka Kogyo Co.) for 75 s and then thoroughly rinsed with running distilled water. For post-exposure baking, the substrate was heated at 120 °C for 3 min using a hot plate. To remove the chromium layer, the substrate was dipped into chromium etching solution [ammonium cerium (IV) sulphate dihydrate $(Ce(NH_4)_4(SO_4)_4 2H_2O)$ and perchloric acid ($HClO_4$) in distilled water] for 2 min. The patterned substrate was etched using the Reactive Ion Etching system (TEP-01; Tateyama Machine Co., Ltd., Toyama, Japan) with SF_6 as an etching gas. The etch conditions used in this study were 20 sccm Ar, 20 sccm SF_6, 0.3 Pa pressure, 0 °C electrode temperature, and 55 W rf power. After etching, the substrate was washed in piranha solution at 180 °C for 30 min, then rinsed thoroughly with running distilled water. The remaining Cr layer was completely removed by dipping into the Cr etching solution. Reservoirs on the substrate were drilled using an ultrasonic driller (Drillmaster SOM-121; Shinodatool Co., Ltd., Okinawa, Japan) and the fabricated substrate was bonded with a quartz cover slip (20 × 20 × 0.5 mm). Prior to the bonding, both quartz substrates were washed with the piranha and SC1 solutions several times. The fabricated substrate and cover slip were attached to each other, pressed at 3.00 N·cm using a digital torque wrench (DTC-N10EXL; Nakamura Mfg. Co., Ltd., Tokyo, Japan), and then dried under vacuum for 12 h. After releasing the force and confirming the lack of interference fringes in the microchannel, an aluminum weight of 75 g was placed on the substrates and heated at 1060 °C for 6 h in a vacuum electric furnace (KDF-75; Denken-Highdental Co., Ltd., Kyoto, Japan).

For fabrication of the nanopillar chips, a chromium layer of about 30 nm was deposited on the washed quartz substrate using the EIS-200ERT-YN system (Elionix Inc., Tokyo, Japan) equipped with electron cyclotron resonance. A positive type electron beam (EB) resist, ZEP520A (Zeon Corporation, Tokyo, Japan), was spin coated at 500 rpm for 5 s followed by 5000 rpm for 60 s. After heating the substrate at 180 °C for 3 min on a hot plate to completely evaporate solvents in the EB resist and stabilizer, the EB resist was exposed to delineate the DLD pattern using the EB ENB-50HS system (Elionix Inc.). The exposed DLD pattern was developed in *o*-xylene (Wako Pure Chemical Industries, Ltd., Osaka, Japan) for 2 min and dried under nitrogen flow. For post-exposure baking, the substrate was heated at 130 °C for 3 min using a hot plate. To remove the chromium layer, the substrate was etched with an electron cyclotron resonance microwave plasma argon ion shower using the EIS-200ERT-YN system. The substrate patterned by the resist was etched using the TEP-01 reactive ion etching system with SF_6 as an etching gas. The etching conditions used were the same as for micropillar fabrication. Subsequent processes including washing, Cr etching, reservoir fabrication, and bonding were also the same as those for micropillar chips.

Standard sample preparation. A dilution series of KCl solutions was prepared to control the zeta potential of the quartz surface. Conductivity and pH of KCl solutions were measured using a conductivity meter (DS-52; Horiba, Ltd., Kyoto, Japan) prior to use. To measure EOF velocity, fluorescein (Thermo Fisher Scientific, Waltham, MA) and rhodamine B (Tokyo Chemical Industry Co., Ltd., Tokyo, Japan) were used; rhodamine B in particular was adopted because of its unique property as a fluorescent neutral marker to quantify EOF[20]. High concentrations of fluorescein (355 μM) and rhodamine B (374 μM) solutions were used unless otherwise noted. All fluorescent polystyrene beads (a series of Fluoresbrite® YG Microspheres) were purchased from Polysciences, Inc (Warrington, PA).

EV preparation. MDA-MB-231 cells were cultured in Dulbecco's modified Eagle's medium (Lonza Japan Ltd., Tokyo, Japan) supplemented with 10% (v/v) exosome-depleted fetal bovine serum (FBS; Exo-FBS™; System Biosciences, Palo Alto, CA) in a humidified atmosphere of 95% air and 5% CO_2 at 37 °C. EVs released from cultured MDA-MB-231 cells were then collected by filtering the culture medium through a 0.22-μm membrane filter to remove contaminants, followed by ultracentrifugation at 110,000 × *g* for 80 min at 4 °C (CS150FNX; Hitachi Koki Co., Ltd., Tokyo, Japan). The supernatant was then aspirated and the pellets were suspended in phosphate buffered saline (pH = 7.2; Wako Pure Chemical Industries, Ltd.) or MilliQ water. Subsequently, ultracentrifugation was performed again under the same conditions as mentioned above. For FE-SEM (Supra 40VP; Carl Zeiss, Oberkochen, Germany), the resulting EV-containing pellets were fixed in 2% paraformaldehyde (Wako Pure Chemical Industries, Ltd.) for 5 min, dispersed on a silicon wafer, and then a gold thin film was sputter-deposited at 2.5 nm thickness. For separation experiments, the resulting pellets were stained with PKH26GL (PKH26 Red Fluorescent Cell Linker Kit for General Cell Membrane Labelling; Sigma-Aldrich, St. Louis, MO) according to manufacturer's instructions. After the two ultracentrifugation steps, the PKH26GL-stained EV-containing pellets were dissolved in MilliQ water and used for the separation experiments.

Direct observation. To observe EOF profiles and transportation behaviors of the fluorescent polystyrene beads and the fluorescently labelled EVs in the DLD device, an inverted fluorescence microscope (Eclipse TE300; Nikon Instech Co., Ltd., Tokyo, Japan) equipped with a 488 nm laser (FLS-448-20; Sigma Koki Co., Ltd., Tokyo, Japan) and EB-CCD camera (C7190-43; Hamamatsu Photonics K. K., Hamamatsu, Japan) was used. Fluorescence images were recorded on HDV tapes using an HDV recorder (HVR-M35J; Sony, Tokyo, Japan) and transferred to an HDD for image processing offline. EOF and bead velocities were analyzed using image analysis software (Cosmos32; Library, Tokyo, Japan). Electric fields were applied through the Pt electrode using a high voltage sequencer (HVS448 1500; LabSmith, Inc., Livemore, CA). For specific use to trace bead and EV

trajectories for enhancing the signal-to-noise ratio, a pre-centered fiber illuminator (C-HGFI Intensilight; Nikon Instech Co., Ltd.) and EM-CCD camera (C9100-23B; Hamamatsu Photonics K. K.) were used by adjusting exposure time. The collected samples after passing the nanopillar array were observed by FE-SEM while EV diameters were measured using Image J (NIH, Bethesda, MD).

RESULTS AND DISCUSSION

EOF velocity measurements. EOF velocity in the straight microchannel was measured using two markers, fluorescein and rhodamine B (Supplemental Figure S3a, b). After the simple straight channel was filled with MilliQ water or KCl solution, these markers were added to one reservoir and the electric field was applied. The velocities of each marker were measured based on observation of the moving boundary between the marker and water or KCl solution as shown in Supplemental Movie S1. The plots in Supplemental Figure S3C clearly show different marker behavior depending on KCl concentration. Whereas the velocity of rhodamine B appeared stable under a wide KCL concentration range of 1 nM to 0.1 M and even in pure water, the migration direction of fluorescein was reversed around the KCl concentration of 1 mM (Supplemental Figure S3C). This result suggests that transportation of fluorescein in the microchannel is simply determined by the balance (or summation) between EOF and electrophoresis because the carboxyl group is always dissociated and negatively charged under neutral pH conditions. In pure water or low KCL concentrations (< 10 μM), strong EOF defeats the electrophoretic force exerted on fluorescein and the marker can move from the anode toward the cathode. However, the electrophoretic force becomes predominant at high KCL concentrations (> 10 mM) because the surface charge of the quartz microchannel is masked by potassium ions and the velocity of the EOF is reduced. An equilibrium point of EOF and electrophoresis against fluorescein was observed at 1 mM KCl. Under this condition, we could not observe any stable boundary movement or measure the velocity.

Compared with fluorescein, rhodamine B exhibited stable behavior under a wide ionic concentration in solution (Supplemental Figure S3C), likely due to rhodamine B being a zwitterion and behaving as a neutral marker reflecting EOF behavior without losing solubility in water. Moreover, the velocity of rhodamine B gradually decreased in a KCl dose-dependent manner, which is equivalent to the solution conductance shown in Supplemental Figure S3D, as indicated by EOF theory[21, 22]. Accordingly, the velocity appeared lower in pure water than in KCl solution, because the high concentration of rhodamine B (374 μM) used in the present study is electrostatically attracted to the dissociated silanol group on the surface of the quartz microchannel and tightly binds in place of potassium ions (0 M) and protons (0.1 μM at pH = 7). As a result, the large hydrophobic group in rhodamine B may screen the electrostatic effect from the negatively charged surface and reduce EOF velocity.

EOF profiles in the DLD device obtained using the simple straight channel described above were observed via fluorescence microscopy. Rhodamine B was loaded from reservoir A to the micropillar array region by applying positive voltage to reservoir A and B while grounding reservoir C and D. As shown in Figure 2C and D, the behavior of rhodamine B at the inlet-sided junction of the microchannels was observed under different voltage conditions. When the applied voltage of reservoir B was larger than reservoir A as shown in Figure 2C, the EOF from reservoir A was squeezed by the EOF from reservoir B owing to the faster EOF in the microchannel loaded from reservoir B. In contrast, when a lower voltage was applied to reservoir B, the EOF in the microchannel loaded from reservoir A swept out to the whole micropillar array region (Figure 2D). Although the physical mechanism of the concentrated boundary formation along the lower edge is still unclear, there were no influence on controlling the flow of nanoparticles and EVs. These results suggest that the EOF profile, including the flow velocity and direction in the micropillar array region, can be easily controlled by adjusting the electric field. Furthermore, the flow was stable over a few hours. When a mixed sample of different sizes was loaded from reservoir A and the voltage ($V_B > V_A > V_C = V_D$) applied, a stable and squeezing liquid flow inside the micropillar array was expected to focus the sample streamline for sample loading, realizing continuous separation based on DLD principles.

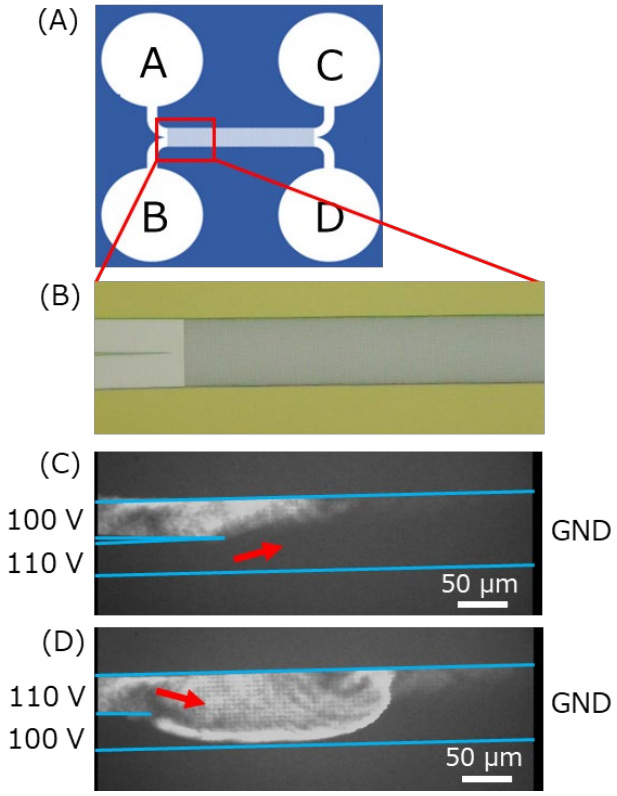

Figure 2. EOF in the micropillar array visualized using the fluorescent neutral marker rhodamine B. (A) Channel design and (B) magnified optical microscope image around the interface between the microchannel and the pillar array. (C, D) Fluorescence images of rhodamine B around the interface under the indicated voltage conditions . Red arrows indicate the direction of net EOF. The sample in reservoir A can be hydrodynamically focused under the condition in (C) and then sample separation can be achieved as in (D). GND, ground.

Separation of fluorescent polystyrene beads by micropillar array chips. Both micro- and nanopillar array geometries were designed based on the theoretical prediction of Inglis et al.[23], following the design and nature of particle separation in micropillar arrays based on the DLD originally proposed in 2004 by Huang et al.[14] Briefly, the pillar-to-pillar spacing (λ),row shift fraction (ε),gap size between pillars (g),

and a migration angle (θ), which is equal to the angle between the pillar-array axis and the microchannel wall axis, are important parameters for determining the critical diameter of a particle (D_c). In the theoretical prediction, D_c is phenomenologically given by,

$$D_c = 2\beta \quad (1)$$

where β is the width of the first streamline that determines the particle path in bumping mode or zigzag mode. This β can be replaced by the gap size between pillars g, the row shift fraction ε, and the variable parameter η to accommodate for non-uniform flow through the pillar gap as follows,

$$D_c = 2\eta g\epsilon \quad (2)$$

Based on this equation, the above parameters were calculated for fabrication of the micro- and nanopillar arrays. The final geometries of the micro- and nanopillar arrays for the following separation experiments are shown in Supplemental Figures S1 and S2, respectively.

Prior to the separation experiments, trajectories of the 500, 300, and 200 nm diameter fluorescent beads were analyzed as shown in Supplemental Figure S4, S5, and S6, respectively. The trajectories were observed using the EM-CCD camera with an exposure time of 5 s around the upstream and downstream region. In the case of 500 and 300-nm beads (Supplemental Figure S5 and S6), the fluorescent beads loaded from reservoir A traversed the micropillar array region and almost completely moved into reservoir D. However, the 200 nm diameter fluorescent beads travelled straight, even in the tilted micropillar array region, and rapidly moved into reservoir C. These results suggest that the nominal critical diameter D_c, which constitutes a boundary of two modes of molecular transport (zigzag and bumping), was not identical to the empirical prediction of DLD driven by pressure flow[23]. This may be due to a difference in the driving scheme of bead transport in the micropillar array region, hydrodynamic pressure, or EOF-driven flow. As Inglis et al.[23] also qualitatively expected in their paper, in the unique case where the flow profile becomes uniform across the gap-like plug flow, the η parameter in equation (**2**) would be unity. As a result, D_c/g would be expected to have a smaller value compared with that of a conventional parabolic flow profile even at the same ε value. Therefore, the above trajectory of the 300-nm fluorescent beads in bumping mode is understandable. In our quantitative estimation based on equation (**2**), the η value was approximately 2.5—which provides D_c = 250 nm—and not the 1.0 predicted by Inglis et al.[23] in the plug flow profile. A precise D_c value may require further scrutiny of the EOF-driven fluid streamline because the flow profile does not reflect the perfect plug flow in the pillar region theoretically assumed by Inglis et al.[23] as the cross-sectional area is continuously altered along the streamline; furthermore, the hydrodynamic pressure change cannot be ignored even under an EOF-driven flow profile.

For separation of the model fluorescent polystyrene bead samples, D_c was set at approximately 400 nm and the micropillar array was fabricated. To elucidate the separation by EOF-driven DLD, a mixture of 200 and 500 nm diameter fluorescent polystyrene beads was loaded from reservoir A and the voltage applied under the same conditions as mentioned above. The trajectories of the fluorescent beads were observed using the EM-CCD camera with an exposure time of 5 s around the upstream and downstream region. As shown in Figure 3, the mixed sample was squeezed toward the upper side of the micropillar array region at the inlet-sided junction, then two streamlines flowing into reservoirs C and D were observed at the outlet-sided junction. Bright spots were only sparsely observed, indicative of the low, non-specific adsorption of the fluorescent beads. After 30 min of separation, 2 μL of solution in reservoirs C and D was sucked out by a pipette and dispersed onto a silicon wafer for FE-SEM. The histograms in Figure 3C, D show the diameter of the observed beads from reservoirs C and D, respectively. Only a few beads of unintended sizes were observed, whereas almost all of the 200 and 500 nm diameter beads were transferred into reservoirs C and D, respectively, based on DLD principles.

Under the gradient of the electric field created by insulating micro- and nanopillar arrays in direct current (DC) electric fields, sub-micron polystyrene beads will exhibit electrophoretic and dielectrophoretic behaviours[24]. Therefore, transportation of the sub-micron polystyrene beads is achieved by the superposition of electrophoresis, electroosmosis, and dielectrophoresis. Considering the high velocities of the polystyrene beads (Table S1), EOF may be a dominant factor in the transportation of these beads. This can be attributed to the bead properties, as they are relatively small (< 500 nm) with low surface charge density (< 20 mC/m^2; predicted value[25-29]). The exerted DEP force, which is described in the Supporting Information, depends on the bead diameter cubed and the gradient of the electric field squared. Because the direction of the DEP force is perpendicular to the electric field line, it may affect the separation efficiency, which will be discussed later.

Another potential factor affecting the separation efficiency is the Debye length (κ^{-1}), which ranges from 30 to 0.4 nm in NaCl solutions of 0.1 to 500 mM, respectively[30]. Jacobson et al.[30] experimentally proved how the κh value (h, half-depth or half-width of the nanochannels) affects the EOF profile in nanofluidic channels. For $\kappa h > 100$, the EOF profile was a plug flow and the electroosmotic mobilities were linear with κh. For the nanopillar chips, κh was larger than 100, even when filled with pure water because the dimensions of the nanopillar spacing are sufficiently large; the half-depth and half-width were 328 nm and 415 nm, respectively. Thus, the EOF profile can be regarded as a plug flow and the Debye layer did not affect the flow profile of the nanopillar chips. Several works involving the separation of small ions in nanofluidic channels were demonstrated using pressure-driven flow and/or EOF[31]. However, the separation targets were small molecules, such as Alexa 488 and rhodamine B[32], compared with that of the Debye length, while the channel dimension was comparable to the Debye length, which is generally < 200 nm. Therefore, the Debye layer may not affect the transport mechanism in a large nanopillar spacing system (830 nm).

Separation of fluorescent polystyrene beads by nanopillar array chips. The mixture of 50 and 200 nm diameter beads was loaded from reservoir A and the voltage was applied under the same conditions mentioned above. Trajectories of the fluorescent beads were observed using the EM-CCD camera with an exposure time of 1 s around the upstream and downstream region as shown in Figure 4A, B. Reservoirs C and D were observed using fluorescence microscopy after separation; as a result, uniformly scattered fluorescence and sparse bright spots were seen as shown in Figure 4C and D, respectively. This different appearance of fluorescence signals may be derived from the size difference of the collected fluorescent beads. Moreover, as shown in Figure

4E and F, FE-SEM of the collected fluorescent beads indicates that 50 and 200 nm diameter beads were mainly collected at reservoirs C and D, respectively, although a small quantity of 50 nm beads were found in reservoir D. This may be due to

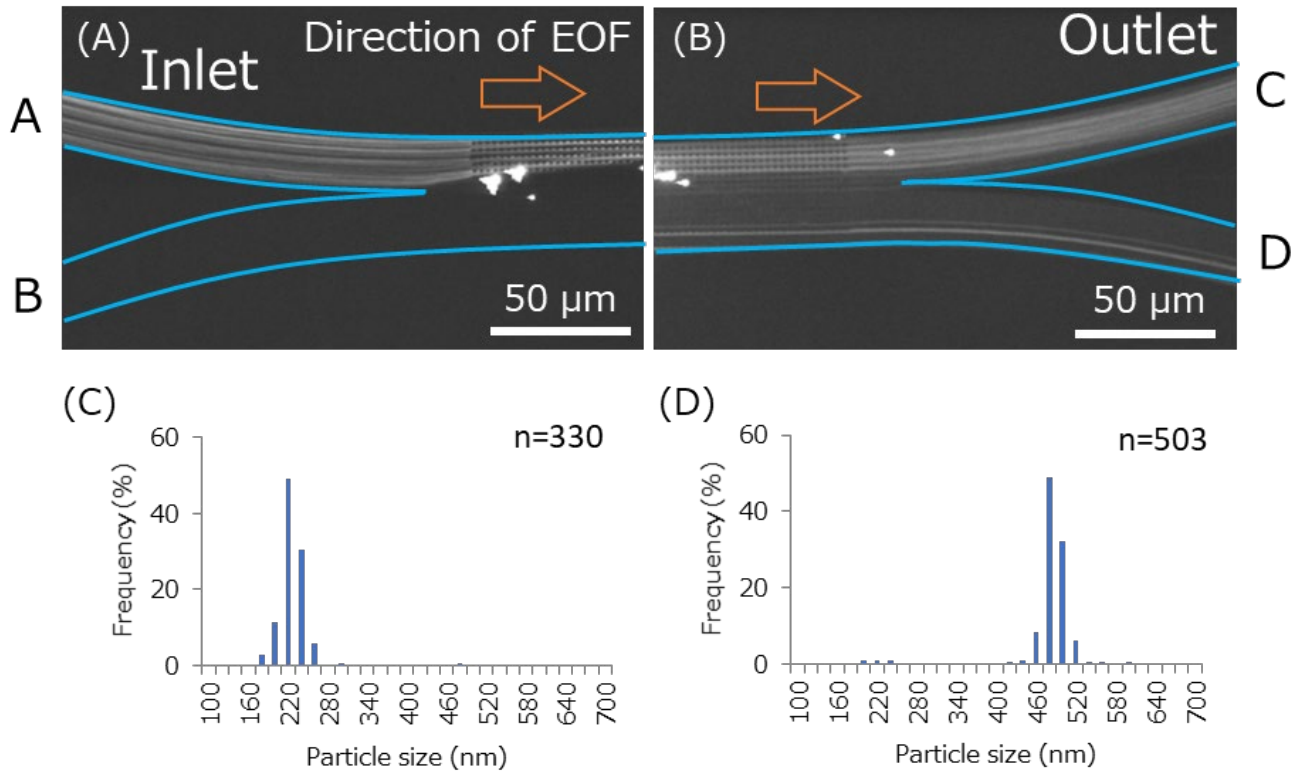

Figure 3. Separation of the 200 and 500-nm fluorescent bead mixture by the micropillar chip. (A) Fluorescence images upstream and (B) downstream of the micropillar array. The samples were loaded from reservoir A and then separated samples were collected from reservoirs C and D, followed by analysis via FE-SEM as shown in (C) and (D), respectively.

thermal diffusion of the 50-nm beads during transportation in the nanopillar array region, as discussed below.

Separation throughput and efficiency of micro- and nanopillar array chips. To estimate the throughput of the devices, fluorescent bead trajectories were tracked and velocities calculated as shown in Table S1. These measured velocities were in the 450–950 μm/s range at 100 V regardless of whether micropillar or nanopillar arrays were used, suggesting that flow velocities are roughly the same under the same voltage conditions. Although the space between the micropillars is three times larger than that between the nanopillars, the bead velocities were in the same range. Considering bead diameter and concentration, the velocities exhibited a linear relationship with the solution volume excluded from the pillars and beads. This result suggests that EOF velocity in the pillar arrays does not solely depend on counterion velocity on the surface under an external electric field but partially consists of parabolic flow. The frequency of particles passing through the micro- or nanopillar array region was almost proportional to the input concentration in the reservoir. Flow rate in the micro- and nanopillar arrays was estimated as a few nL/min and sub-nL/min, respectively. The nanopillar array flow rate was comparable to the one previously reported by Wunsch et al.[19] They used a nanopillar array with gap ranging from 42 to 235 nm inside a microchannel 36 μm in width and 360 μm in length, through which a volumetric flow rate of 0.1–0.2 nL/min was achieved by applying an input pressure of 200–800 kPa. Considering that the maximum applicable pressure of a syringe pump is generally a few MPa when a μL-syringe is used, the above value achieved by the device fabricated by Wunsch et al.[19] is almost the strongest available pressure, which permits few further design flexibilities, such as extension of channel length or gap shrinkage. In comparison, the device used herein, with a nanopillar array gap of 830 nm inside a microchannel 30 μm in width and 1.38 mm in length, generated a flow rate of 0.3 nL/min by only applying 100 V and no pressure. Notably, this lack of pressure occurred even though the pressure drop from the inlet to the outlet could be estimated as 120 kPa by the sum of pressure drops at the microchannel ΔP region and the nanopillar array R based on the following equations,

$$\Delta P = \frac{12\mu L}{wh^3} Q \quad (3)$$

$$R = \frac{4.6\mu L}{wG^2 h} \quad (4)$$

where μ is the viscosity of the solution, G is the pillar gap, Q is the flow rate, L is the length of the channel, h is the height of the channel, and w is the width of the channel. This pressure-free EOF-driven device provides a considerable advantage because the previously reported pressure-driven DLD device requires a strong bond between the substrate and coverslip; e.g., an extended annealing step at 500 °C for 24 h[19], along with perfect tube fitting to tolerate the strong pressure.

Separation efficiency of the separation column was evaluated based on the definition of the displacement efficiency

described previously[19]. The displacement efficiency H is defined as,

$$H = \frac{\Delta w}{w} = \frac{\tan\theta}{\tan\theta_{max}} \quad (5)$$

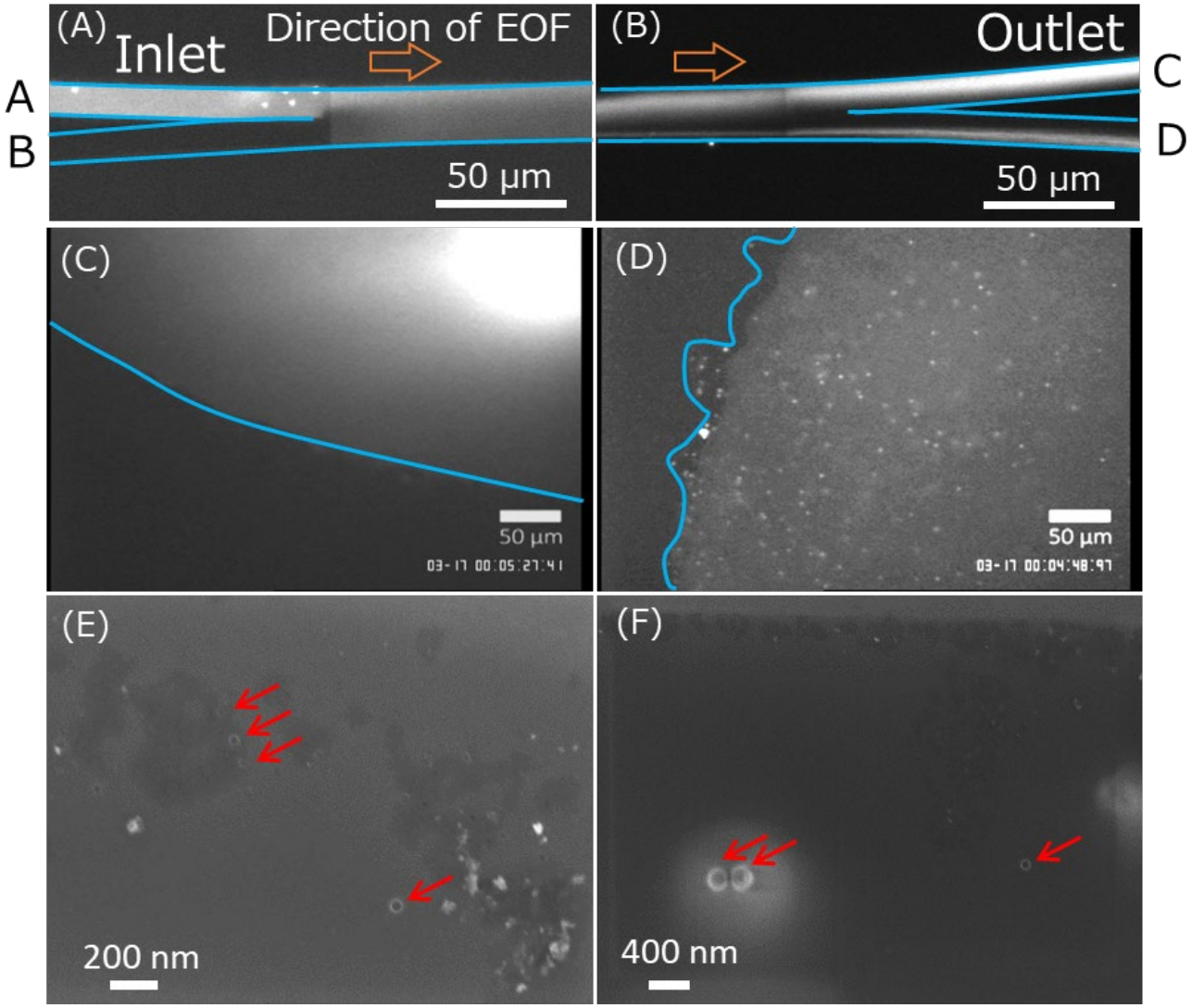

Figure 4. Separation of the 50 and 200-nm fluorescent bead mixture by the nanopillar chip. (A, B) Fluorescence images upstream (A) and downstream (B) of the nanopillar array. The samples were loaded from reservoir A. After separation, reservoir C and D were analyzed with a fluorescence microscope as shown in (C) and (D), respectively. Reservoir boundaries are indicated with the blue line. Separated samples were collected from reservoirs C and D by a pipette, then observed using SEM as shown in (E) and (F), respectively.

where Δw is the lateral displacement, θ is the migration angle of the objects along the channel, and $\tan\theta = \Delta w/L$, θ_{max} is the maximum angle corresponding to the angle between the pillar array and the channel. This equation suggests that the percentage of the displacement angle indcates the dominant mode of the migration whether it is a zigzag or bumping mode. As shown in Table 1, the displacement efficiencies of 300 and 100-nm beads, which are the closest values to the nominal critical value D_c in the micropillar and nanopillar array, respectively, were considerably lower than the intended values. This may occur due to thermal diffusion of the beads. Furthermore, the retracting DEP force toward the nanopillars may enhance the lateral displacements derived from the zigzag mode; as a result, bead streamlines would be broadened and the displacement efficiencies lost. Considering the time required by the beads to traverse the nanopillar and micropillar array region along the migration direction, the maximum vertical diffusion distance of the beads across the migration direction was calculated as 5.1 μm in 3 s and 5.3 μm in 10 s for the 100 nm and 300-nm beads, respectively, at 20°C in the respective arrays. Therefore, thermal diffusion does not appear to be critical for the separation of 300-nm beads in the micropillar chip compared with the behavior of 100-nm beads in the nanopillar chip, which only contains 30 μm wide microchannels.

Separation of EVs by nanopillar array chips. The nanopillar chip, which demonstrated the ability to separate nm-sized beads, was employed to separate EVs extracted from the culture medium of MDA-MB-231 human breast cancer cells. EVs extracted by the ultracentrifugation method were separated using the nanopillar chip as shown in Figure 5. Fluorescent spots observed in Figure 5A, B indicate EVs stained with PKH. Owing to the low concentration of input EVs, EVs were difficult to observe especially downstream of the nanopillar array region. Therefore, the fractions in reservoirs C and D were collected and confirmed by FE-SEM. The collected sample from reservoir C, which is expected to fractionate exosomes < 130 nm in diameter, showed small vesicles 50–400 nm in diameter (Figure 5C). In comparison, large aggregates > 400

nm in diameter were clearly observed in reservoir D (Figure 5D). Considering the separation results and interpretation of the prior experiments using polystyrene beads, the D_c predicted in this EV separation procedure appeared to not be identical to the

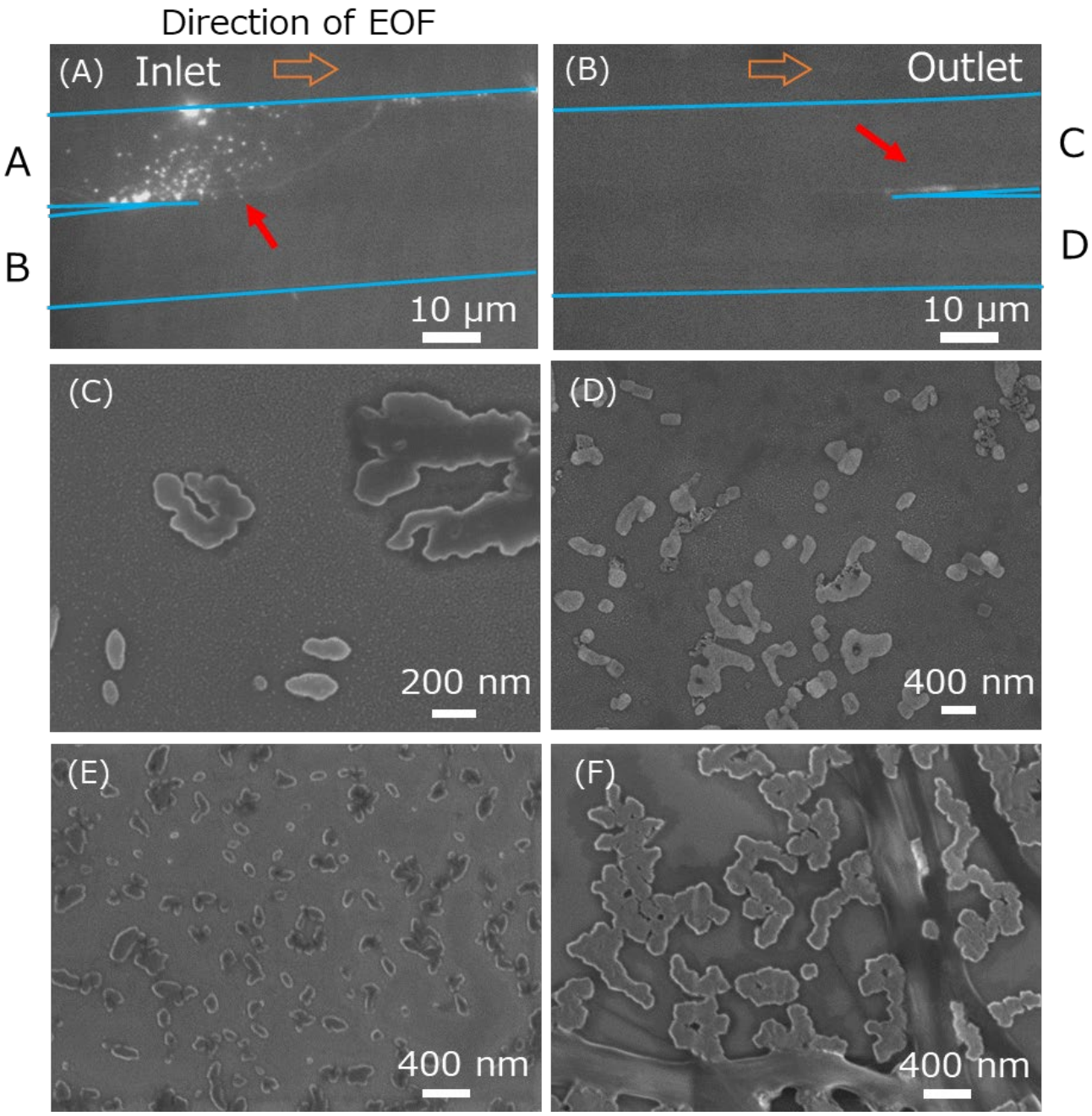

Figure 5. Separation of the EVs by the nanopillar chip. (A, B) Fluorescence images (A) upstream and (B) downstream of the nanopillar array. The red arrows indicate EVs stained with PKH. (C, D) Ultracentrifuged EVs were observed at a different magnification before loading the nanopillar chip. Separated EVs were collected from reservoirs C and D, then observed by SEM as shown in (E) and (F), respectively. Although individual EVs together with some aggregates were observed in (E), only large aggregates were observed in (F).

theoretical estimation or the experimental results of polystyrene beads. This may be due to three main factors, surface charges, densities, and flexibilities. In this EOF-driven DLD separation, strong EOF generated in pure water on the quartz surface constitutes a dominant force for transporting the EVs. However, the electrophoretic forces could not be ignored, although the exact electrophoretic force against EVs was difficult to estimate, as the ζ potential and size of individual EVs were unclear. The slight heavy density of EVs (1.16–1.19 g/mL) compared with that of the polystyrene beads (approximately 1.05 g/mL) may also affect the migration behavior in nanopillar chips. In particular, the polymerized particles may be less flexible (i.e., stiffer) than the EVs; therefore, the bumping mode may be advantageous if the particles have the same diameter.

Although the EOF is a dominant factor in the transport of EVs, a relatively strong electric field concentrated in the nanopillar array region—theoretically around 66–72 V/cm—may damage the EV structure. As indicated by Nakase et al.[33], external substances can be transported into EVs based on an electroporation technique. Therefore, we need to carefully

consider the influence on EV structure during separation in future studies.

Table 1. Displacement efficiencies of the various sizes of fluorescent beads calculated by equation (**5**) in the micro- and nanopillar chips.

	Beads diameter (nm)	Displacement efficiency (%)
Micropillar array	500	96
	300	54
	200	3.8
Nanopillar array	200	63
	100	12
	50	0.0

CONCLUSIONS

To perform the EOF-driven DLD, EOF profiles in the micro- and nanopillar chips were optimized to generate sheath flow for sample injection and stable flow for separation in the pillar regions. In this process, the dominant force controlling the behaviors of negatively charged polystyrene particles and EVs was EOF, and not the electrical force, in pure water under an electric field. The complex nanopillar geometry affected the velocity profile of EOF in the pillar arrays and partially consisted of a parabolic velocity profile. This continuous separation technique is expected to be useful as a new platform of EV separation and enrichment because of its easy-to-operate technique.

ASSOCIATED CONTENT

Supporting Information

The Supporting Information is available free of charge on the ACS Publications website.

Design details of micro- and nanopillar chips, EOF velocities in the straight microchannel, trajectories of fluorescent beads with different sizes in micro- and nanopillar chips (PDF).

EOF velocity measurements (wmv).

AUTHOR INFORMATION

Corresponding Author

*E-mail: kaji@cstf.kyushu-u.ac.jp

Author Contributions

All authors have given approval to the final version of the manuscript.

Notes

The authors declare no competing financial interest.

ACKNOWLEDGMENTS

This work was partially supported by JST/PRESTO [grant number JPMJPR16F4, JPMJPR151B], Grant-in-Aid for Scientific Research on Innovative Areas [18H04545], Nanotechnology Platform Program (Molecule and Material Synthesis) of the Ministry of Education, Culture, Sports, Science and Technology (MEXT), a JSPS Grant-in-Aid for Scientific Research (A) [16H0209], the ImPACT Program of the Council for Science, Technology and Innovation (Cabinet Office, Government of Japan), and a research grant from the Nitto Foundation.

REFERENCES

(1) Graner, M. W.; Alzate, O.; Dechkovskaia, A. M.; Keene, J. D.; Sampson, J. H.; Mitchell, D. A.; Bigner, D. D. Proteomic and immunologic analyses of brain tumor exosomes. *FASEB J.* **2009**, *23*, 1541–1557.

(2) Simpson, R. J.; Lim, J. W.; Moritz, R. L.; Mathivanan, S. Exosomes: proteomic insights and diagnostic potential. *Expert Rev. Proteomics* **2009**, *6*, 267–283.

(3) Mathivanan, S.; Fahner, C. J.; Reid, G. E.; Simpson, R. J. ExoCarta 2012: database of exosomal proteins, RNA and lipids. *Nucleic Acids Res.* **2012**, *40*, D1241–1244.

(4) Valadi, H.; Ekstrom, K.; Bossios, A.; Sjostrand, M.; Lee, J. J.; Lotvall, J. O. Exosome-mediated transfer of mRNAs and microRNAs is a novel mechanism of genetic exchange between cells. *Nat. Cell Biol.* **2007**, *9*, 654–659.

(5) Skog, J.; Wurdinger, T.; van Rijn, S.; Meijer, D. H.; Gainche, L.; Sena-Esteves, M.; Curry, W. T., Jr.; Carter, B. S.; Krichevsky, A. M.; Breakefield, X. O. Glioblastoma microvesicles transport RNA and proteins that promote tumour growth and provide diagnostic biomarkers. *Nat. Cell Biol.* **2008**, *10*, 1470–1476.

(6) Yasui, T.; Yanagida, T.; Ito, S.; Konakade, Y.; Takeshita, D.; Naganawa, T.; Nagashima, K.; Shimada, T.; Kaji, N.; Nakamura, Y.;

Thiodorus, I. A.; He, Y.; Rahong, S.; Kanai, M.; Yukawa, H.; Ochiya, T.; Kawai, T.; Baba, Y. Unveiling massive numbers of cancer-related urinary-microRNA candidates via nanowires. *Science Advances* **2017**, *3*.

(7) Balaj, L.; Lessard, R.; Dai, L.; Cho, Y. J.; Pomeroy, S. L.; Breakefield, X. O.; Skog, J. Tumour microvesicles contain retrotransposon elements and amplified oncogene sequences. *Nat. Commun.* **2011**, *2*, 180.

(8) Vagner, T.; Spinelli, C.; Minciacchi, V. R.; Balaj, L.; Zandian, M.; Conley, A.; Zijlstra, A.; Freeman, M. R.; Demichelis, F.; De, S.; Posadas, E. M.; Tanaka, H.; Di Vizio, D. Large extracellular vesicles carry most of the tumour DNA circulating in prostate cancer patient plasma. *J. Extracell. Vesicles* **2018**, *7*, 16.

(9) Sharma, A.; Khatun, Z.; Shiras, A. Tumor exosomes: cellular postmen of cancer diagnosis and personalized therapy. *Nanomedicine* **2016**, *11*, 421–437.

(10) Rekker, K.; Saare, M.; Roost, A. M.; Kubo, A.-L.; Zarovni, N.; Chiesi, A.; Salumets, A.; Peters, M. Comparison of serum exosome isolation methods for microRNA profiling. *Clinical Biochemistry* **2014**, *47*, 135–138.

(11) Lobb, R. J.; Becker, M.; Wen Wen, S.; Wong, C. S. F.; Wiegmans, A. P.; Leimgruber, A.; Möller, A. Optimized exosome isolation protocol for cell culture supernatant and human plasma. *J. Extracell. Vesicles* **2015**, *4*, 27031.

(12) De Toro, J.; Herschlik, L.; Waldner, C.; Mongini, C. Emerging roles of exosomes in normal and pathological conditions: new insights for diagnosis and therapeutic applications. *Front. Immunol.* **2015**, *6*, 203.

(13) Lane, R. E.; Korbie, D.; Anderson, W.; Vaidyanathan, R.; Trau, M. Analysis of exosome purification methods using a model liposome system and tunable-resistive pulse sensing. *Sci. Rep.* **2015**, *5*, 7639.

(14) Huang, L. R.; Cox, E. C.; Austin, R. H.; Sturm, J. C. Continuous particle separation through deterministic lateral displacement. *Science* **2004**, *304*, 987–990.

(15) Holm, S. H.; Beech, J. P.; Barrett, M. P.; Tegenfeldt, J. O. Separation of parasites from human blood using deterministic lateral displacement. *Lab Chip* **2011**, *11*, 1326–32.

(16) Ranjan, S.; Zeming, K. K.; Jureen, R.; Fisher, D.; Zhang, Y. DLD pillar shape design for efficient separation of spherical and non-spherical bioparticles. *Lab Chip* **2014**, *14*, 4250–4262.

(17) Davis, J. A.; Inglis, D. W.; Morton, K. J.; Lawrence, D. A.; Huang, L. R.; Chou, S. Y.; Sturm, J. C.; Austin, R. H. Deterministic hydrodynamics: taking blood apart. *Proc. Natl. Acad. Sci. U. S. A.* **2006**, *103*, 14779–14784.

(18) Okano, H.; Konishi, T.; Suzuki, T.; Suzuki, T.; Ariyasu, S.; Aoki, S.; Abe, R.; Hayase, M., Enrichment of circulating tumor cells in tumor-bearing mouse blood by a deterministic lateral displacement microfluidic device. *Biomed. Microdevices* **2015**, *17*, 9964.

(19) Wunsch, B. H.; Smith, J. T.; Gifford, S. M.; Wang, C.; Brink, M.; Bruce, R. L.; Austin, R. H.; Stolovitzky, G.; Astier, Y. Nanoscale lateral displacement arrays for the separation of exosomes and colloids down to 20 nm. *Nat. Nano.* **2016**, *11*, 936–940.

(20) Milanova, D.; Chambers, R. D.; Bahga, S. S.; Santiago, J. G. Electrophoretic mobility measurements of fluorescent dyes using on-chip capillary electrophoresis. *Electrophoresis* **2011**, *32*, 3286–3294.

(21) Burgreen, D.; Nakache, F. R. Electrokinetic Flow in Ultrafine Capillary Slits1. *J. Phys. Chem.* **1964**, *68*, 1084–1091.

(22) Rice, C. L.; Whitehead, R. Electrokinetic Flow in a Narrow Cylindrical Capillary. *J. Phys. Chem.* **1965**, *69*, 4017–4024.

(23) Inglis, D. W.; Davis, J. A.; Austin, R. H.; Sturm, J. C. Critical particle size for fractionation by deterministic lateral displacement. *Lab Chip* **2006**, *6*, 655–658.

(24) Cummings, E. B.; Singh, A. K. Dielectrophoresis in microchips containing arrays of insulating posts: Theoretical and experimental results. *Anal. Chem.* **2003**, *75*, 4724–4731.

(25) Srivastava, S. K.; Gencoglu, A.; Minerick, A. R. DC insulator dielectrophoretic applications in microdevice technology: a review. *Anal. Bioanal. Chem.* **2011**, *399*, 301–321.

(26) Ozuna-Chacon, S.; Lapizco-Encinas, B. H.; Rito-Palomares, M.; Martinez-Chapa, S. O.; Reyes-Betanzo, C. Performance characterization of an insulator-based dielectrophoretic microdevice. *Electrophoresis* **2008**, *29*, 3115–3122.

(27) Ohsawa, K.; Murata, M.; Ohshima, H. Zeta-Potential and Surface-Charge Density of Polystyrene-Latex - Comparison with Synaptic Vesicle and Brush-Border Membrane Vesicle. *Colloid Polym. Sci.* **1986**, *264*, 1005–1009.

(28) Martinez-Lopez, J. I.; Moncada-Hernandez, H.; Baylon-Cardiel, J. L.; Martinez-Chapa, S. O.; Rito-Palomares, M.; Lapizco-Encinas, B. H. Characterization of electrokinetic mobility of microparticles in order to improve dielectrophoretic concentration. *Anal. Bioanal. Chem.* **2009**, *394*, 293–302.

(29) Green, N. G.; Morgan, H. Dielectrophoresis of submicrometer latex spheres. 1. Experimental results. *J. Phys. Chem. B* **1999**, *103*, 41–50.

(30) Haywood, D. G.; Harms, Z. D.; Jacobson, S. C. Electroosmotic Flow in Nanofluidic Channels. *Anal. Chem.* **2014**, *86*, 11174–11180.

(31) Gillespie, D.; Pennathur, S. Separation of Ions in Nanofluidic Channels with Combined Pressure-Driven and Electro-Osmotic Flow. *Anal. Chem.* **2013**, *85*, 2991–2998.

(32) Garcia, A. L.; Ista, L. K.; Petsev, D. N.; O'Brien, M. J.; Bisong, P.; Mammoli, A. A.; Brueck, S. R. J.; López, G. P. Electrokinetic molecular separation in nanoscale fluidic channels. *Lab Chip* **2005**, *5*, 1271–1276.

(33) Nakase, I.; Futaki, S. *Sci. Rep.* **2015**, *5*, 10112.

Table of Contents artwork

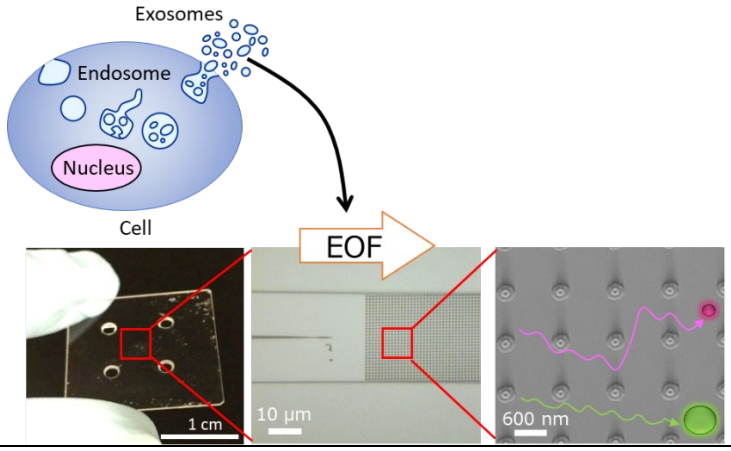
Exosomes
Endosome
Nucleus
Cell
EOF
1 cm
10 μm
600 nm